Accepted for publication in
Chemical Engineering Journal, Dec 2011

Free Surface Electrospinning from a Wire Electrode

Keith M. Forward and Gregory C. Rutledge
Department of Chemical Engineering, Novartis-MIT Center for Continuous Manufacturing, Massachusetts Institute of Technology, Cambridge, MA 02139

Abstract

Electrostatic jetting from a free liquid surface offers an alternative to conventional electrospinning in which jets are emitted from spinnerets. In this work we analyze a system in which a wire electrode is swept (in a rotary motion) through a bath containing a polymeric solution in contact with a high voltage, resulting in entrainment of the fluid, the formation of liquid droplets on the wire and electrostatic jetting from each liquid droplet. Solutions of polyvinylpyrrolidone in ethanol were used as test systems to evaluate each stage of the process. The volume of individual droplets on the wire were measured by photographic methods and correlated with the viscosity, density and surface tension of the liquid, and with system parameters such as electrode rotation rate and wire diameter. The local electric field in the absence of liquid entrainment was modeled using conventional electrostatics, and jet initiation was found to occur consistently at the angular position where the electric field exceeds a critical value of 34 kV/cm, regardless of rotation rate. Two operating regimes were identified. The first is an entrainment-limited regime, in which all of the entrained liquid is jetted from the wire electrode. The second regime is field-limited, in which the residence time of the wire electrode in an electric field in excess of the critical value is too short to deplete the fluid on the wire. The productivity of the system was measured and compared to the theoretical values of liquid entrainment. As expected, highest productivity occurred at high applied potentials and high rotation rates.

Keywords: Electrospinning, Free Surface Electrospinning, Needleless Electrospinning, Nanofibers

1. Introduction

Electrostatic fiber formation, or "electrospinning" has attracted much attention over the past decade as an effective technique for producing submicron fibers and nonwoven mats with remarkable properties. However, one of the perceived drawbacks of the method for industrial purposes is its low production rate. A typical production rate from a single spinneret is 0.1 -1 g of fiber per hour, depending on the solution properties and operating parameters; in general, the smallest fibers are fabricated by reducing the solids content of the spin dope or by reducing the flow rate to the spinneret, both of which lead to lower productivity [1]. Several attempts have been made to use an array of spinnerets to increase productivity [2,3]. These studies are typically characterized by careful attention to the spacing and geometric arrangement of the spinnerets and/or the use of auxiliary electrodes to modify the inter-jet electrical field interactions. For a typical spacing of 1 to 3 nozzles per cm^2, a production rate of 1 kg/hr can be realized, in principle, with a multi-nozzle design on the order of 1 square meter in area. However, these configurations often lead to non-uniform electric fields, resulting in discontinuous operation and poor quality non-woven mats [4-8]. Operational and quality control issues such as nozzle clogging and spatial variation of the jets from nozzle to nozzle are often cited as problems encountered by these approaches.

A remarkable feature of the electrospinning process is that jets can be launched, in principle, from any liquid surface [9]. Thus, a variety of configurations have been reported that produce jets from free liquid surfaces, without the use of a spinneret. These include the use of a magnetic liquid in which "spikes" can be formed to concentrate field lines at points on a liquid surface [10], liquid-filled trenches [9], wetted spheres [11], cylinders [12-14] and disks [14], conical wires [15,16], rotating beaded wires [17] and gas bubbles rising through the liquid

surface [18,19]. In the case involving the use of a magnetic liquid, a jet density as high as 26 jets/cm^2 was reported [10]. Such methods have several potential benefits, including simplicity of design, robustness against clogging of a spinneret, and increased productivity though the simultaneous operation of numerous jets. All of these methods share the feature that liquid jets are launched from a free liquid surface, often with the aid of a device or disturbance that introduces curvature to the liquid interface. We refer to these processes collectively as "free surface electrospinning," although some have been previously described as "needleless electrospinning" [9-16], or "bubble electrospinning" [18,19], for example.

In this report, we analyze the particular case of free surface electrospinning from a thin wire electrode. In this process, a metal wire electrode is swept through an electrified liquid bath in a direction perpendicular to its own axis. Upon exiting the bath through the liquid/air interface, liquid is entrained, resulting in a coating of liquid on the wire. Such coatings are generally unstable and undergo a Plateau-Rayleigh instability, resulting in de-wetting of the liquid film on the wire and the formation of separated droplets of charged liquid on the metal wire; the formation of droplets provides the local curvature desired to facilitate jetting. Given a sufficiently high electric field, the charged liquid drop deforms into a Taylor-like cone and emits a jet. By mounting several wires on a rotating spindle, the processes of immersion, entrainment, de-wetting and jetting can be performed repeatedly in a simple manner. Variations of this basic design have been developed and sold commercially by Elmarco Co. (Elmarco, Libarec, CZ). Here we examine how the liquid properties (i.e. surface tension, viscosity, density and concentration) and the operating parameters of applied electric potential and spindle rotation rate (or wire velocity) affect the productivity of the process, in terms of the sequential steps of entrainment, de-wetting, and jetting.

2. Background

The processes of liquid entrainment on an object as it passes through an interface between two liquids, the breakup of an annular liquid film on a cylinder, and the formation of jets by electrostatic forces are problems that have received more or less attention over the years, in other contexts. Here, we review some of the prior work on each of these problems, in preparation for integrating them into a more complete description of free surface electrospinning from a wire electrode.

2.1 Liquid Entrainment

As a wire travels through a liquid-air interface, the liquid experiences forces due to gravity, surface tension, viscosity and inertia. These forces determine the amount of the liquid entrained on the wire. The forces on the liquid deform the surface (liquid-air interface) such that it first coats the upper hemisphere of the wire. As the wire begins to travel away from the original surface, gravitational forces cause liquid from the upper hemisphere to drain back toward the liquid bath, leading to the development of a thinning film behind the wire, while capillary and viscous forces resist such drainage [20]. This sequence of events is illustrated in Fig. 1.

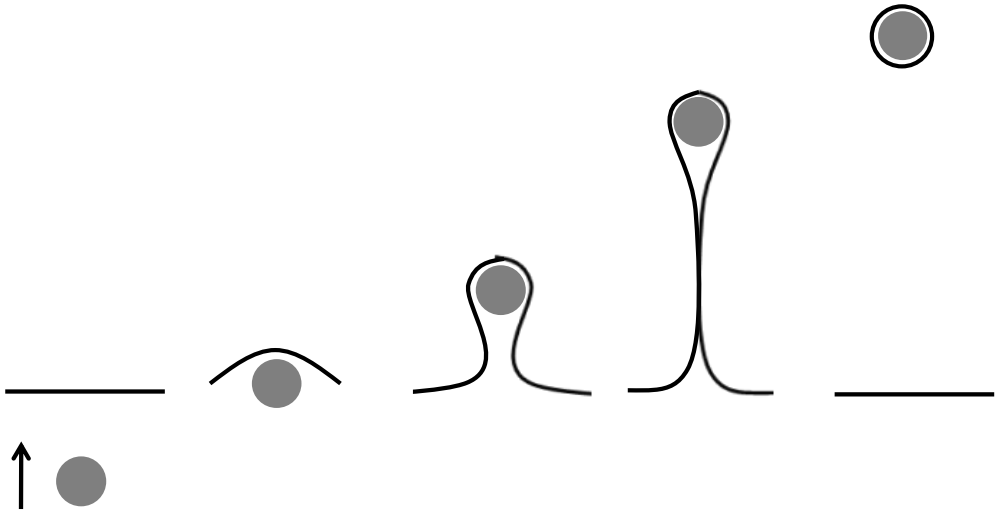

Figure 1. Evolution of the surface profile as a sphere or cylinder (viewed end-on) travels through a liquid interface.

To the best of our knowledge, analysis of a cylinder oriented with its axis parallel to the plane of an interface between two liquids and traveling through the interface has not been reported. However, related geometries have been studied. Spherical particles can be coated by a viscous, dense liquid as they rise under the action of the buoyancy force through the interface with a second, less viscous and less dense liquid [21,22]. Buoyancy forces have been used to coat particles when particles of a lesser density travel from one liquid to another liquid [23]. Several studies have investigated the behavior of a gas bubble traveling through an interface, in a process referred to as "coalescence" [24-26]. Of course, the process of entrainment and draining of a liquid film from a gas bubble as it emerges from a liquid bath is also relevant to those processes described as "bubble electrospinning" [18,19].

Geller *et al.* [24], Manga and Stone [25], and Lee *et al.*[26] each performed simulations of liquid entrainment on a rigid sphere traveling through an interface at low Reynolds number,

$Re = 2u\rho r/\eta < 1$, where u, r, ρ and η are the velocity of the sphere, characteristic length scale (i.e. the radius of the sphere), density and viscosity of the liquid, respectively. Under creeping, or Stokes, flow, the inertial forces are negligible compared to the viscous forces, and liquid entrainment was found to be a function of two dimensionless numbers, the capillary number, $Ca = u\eta/\gamma$, where γ is the surface tension of the interface, and the Bond number, $Bo = \rho g r^2/\gamma$, where g is the gravitational constant (9.8 m/s^2). The capillary number serves as a measure of the viscous force relative to surface force, whereas the Bond number measures gravitational force relative to surface force. As the sphere travels though the interface, a filament of thinning liquid forms behind the sphere until, at a critical thickness, the filament ruptures and recoils, leaving only a thin coating on the sphere. Unfortunately, none of these simulations were carried out to the point of rupture, but it was estimated that rupture of the filament may not occur until the sphere has traveled a distance from the surface several hundred times the radius of the sphere. Therefore, it was not feasible to run a simulation to completion. Nevertheless, these simulations serve to demonstrate that liquid entrainment at low Reynolds number is strongly dependent on the capillary number and weakly dependent on the Bond number. By analogy to the case for the sphere, we expect that liquid entrained on a cylinder is also a function of the capillary and Bond numbers, with entrainment giving rise to a trailing film of liquid rather than a filament.

2.2 De-wetting (Droplet Formation)

After the thinning film ruptures behind the rotating wire, the liquid film recoils and forms an annular liquid film on the wire. Such liquid films undergo a Plateau-Rayleigh instability, resulting in de-wetting and droplet formation along the wire. This problem has been studied by Goren, using a classical stability analysis in which a dispersion relation is obtained that describes

the rate of growth of infinitesimal periodic disturbances of the annular liquid film [27-29]. Droplet breakup on the wire is dominated by the most rapidly growing disturbance, whose wavelength $\lambda = f(a_o, Oh)$ is a function of the radius, a_o, of the free liquid surface on the wire and the Ohnesorge number, $Oh = \eta/(\rho\gamma r)^{0.5}$, of the liquid. At low levels of entrainment ($a_o/r < 2$), the most rapidly growing disturbance has only a weak dependence on the Ohnesorge number; under these conditions, one expects to observe $2\pi a_o/\lambda = 0.69$ (the so-called "wavelength parameter") for all liquids, regardless of viscosity.

2.3 Droplet Shape

In the absence of an external field, liquid droplets on a wire adopt either a symmetrical, "barrel" shape or a nonsymmetrical, "clamshell" shape, depending on the wettability of the wire material and the mode of wetting [31]. In this work we observed exclusively the characteristic symmetrical droplet type in the absence of an applied electric field, as shown in Fig 2. When the diameter of the cylinder is less than the capillary length, $l_{cap} = (\gamma/\rho g)^{1/2}$, the surface tension force dominates over the gravitational force, and the shape of the droplet is found by minimizing the surface free energy [32-33]. Following Carroll, we determine both the volume (V_d) and contact angle (θ) for a liquid on a wire from photographic measurements of the diameter of the droplet at its widest point ($2h$) and the length (l_d) of the droplet, by solving the following set of equations: [31]

$$\begin{aligned} Y^2 &= H^2\left(1 - k^2 \sin^2\varphi\right) \\ X &= \pm\left[bF_e(\varphi, k) + HE_e(\varphi, k)\right] \\ b &= \left(H\cos\theta - 1\right)/\left(H - \cos\theta\right) \\ k^2 &= 1 - b^2/H^2 \\ \sin^2\varphi &= \left(H^2 - 1\right)/kH^2 \end{aligned} \qquad (1a)$$

$$X(Y=1)=\pm\frac{L}{2} \tag{1b}$$

Here, r is the radius of the wire, $Y=y/r$ and $X=x/r$ are scaled coordinates for the profile of the droplet, $H=h/r$ is the scaled maximum height (radius) of the droplet and $L = l_d/r$ is the scaled length of the droplet along the wire. In practice, an initial value for the contact angle θ is assumed and the set of equations in eq. 1(a) is solved iteratively by successive substitution until eq. 1(b) is satisfied. The volume of the droplet is then determined by integrating over the profile of the droplet:

$$V_d = r^3\left\{\frac{2H\pi}{3}\left[\left(2b^2+3Hb+2H^2\right)E_e(\varphi,k)-b^2F_e(\varphi,k)+\left(H^2-1\right)^{1/2}\left(1-b^2\right)^{1/2}\right]-\pi L\right\} \tag{2}$$

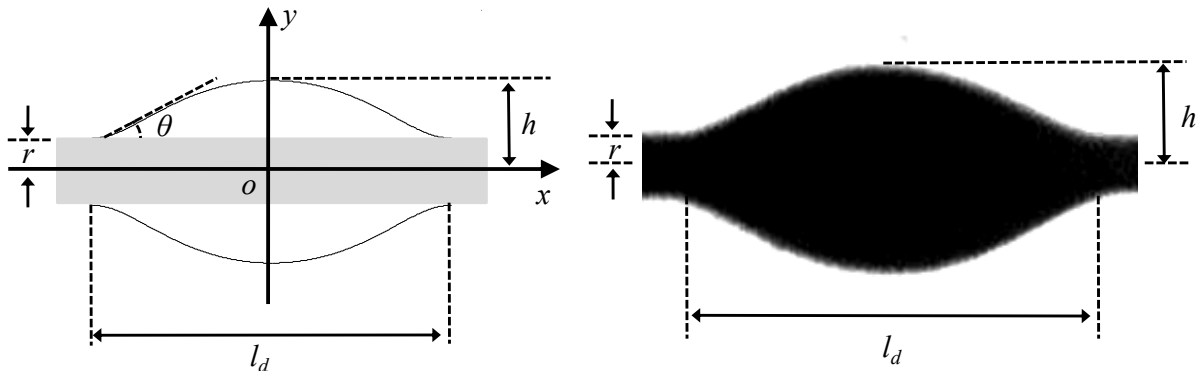

Figure 2. Geometry for determining the profile of symmetrical droplet on a thin cylinder.

2.4 Electrospinning

Conventional electrospinning is typically performed with the use of a nozzle or spinneret to supply fluid to a continuously operating jet, and a static or moving plate or drum is used as the ground electrode upon which fibers are collected. The details of the high voltage and ground electrode configuration affect the shape of the electric field that acts to accelerate the charged fluid, resulting in a slender thinning jet. So-called "point-plate" and "parallel plate"

configurations are most common; in the former, the field lines are strongly curved in the immediate vicinity of the spinneret, whereas in the latter configuration, the field is essentially uniform between the electrodes. Hohman *et al.* first presented a general theory for electrohydrodynamics applicable to the charged fluid jet that captured the competition between varicose and "whipping" instabilities. Significantly, for fluids of finite conductivity, a second varicose mode, dubbed the "conductive" mode, was identified [34-36]. The analysis of Hohman *et al.* is valid for Newtonian fluids; the theory was subsequently extended to non-Newtonian fluids and nonisothermal conditions by several investigators [37-39]. The solutions used in electrospinning are described as "leaky dielectrics" – poorly conducting liquids in which a finite ionic charge density can be induced at their interfaces with other fluids, for example in the presence of an electric field. Such surface charges modify the local electric field and result in electrical stresses that differ from those present in perfect conductors or dielectrics. For example, Hohman *et al.* showed that strong electric fields serve to stabilize the Rayleigh mode while destabilizing the whipping mode. In the current context, it is noteworthy that they identified a threshold electric field for stable jetting in the limit of low flow rate, for an inviscid, perfect conductor: $\left(\varepsilon-\varepsilon_0\right)E_\infty^2=\left(2\pi\gamma\right)/r_0$ [34]. Subsequently, Fridrikh et al [40] and Helgeson et al [41] developed relations to correlate the "terminal" jet diameter and the experimentally observed jet diameter, respectively, with fluid and operating parameters of the electrospinning jet. Prominent among these parameters is the ion charge density on the surface of the jet, which can be estimated from measurements of the volumetric flow rate of the jet, Q, the electric current, I, and the diameter of the jet. Following the work of Gañán-Calvo [42], Bhattacharjee *et al.* demonstrated empirically that, under certain conditions, $I\sim EQ^{0.5}K^{0.4}$, where K is the conductivity of the polymer solution [43]. All of these works were certainly developed with the conventional

spinneret-based configuration in mind, but the physics behind the induction of surface charge in the presence of an electric field and consequent generation of electrical stresses should be roughly transferable to jets emitted from free liquid surfaces as well.

Lukas *et al.* have modeled the initiation of jetting from the planar free surface of a perfectly conducting liquid as a surface wave instability[9]. This model predicts that a critical electric field strength exists above which electrostatic forces overwhelm capillary forces to make the liquid surface unstable. This critical electric field is given by the following relation:

$$E_J = \sqrt[4]{4\gamma\rho g / \varepsilon^2} \ . \tag{3}$$

ε is the permittivity of the ambient gas. Above this critical electrical field, electrospinning jets are predicted to emit spontaneously from a planar liquid surface. Similar to the Plateau-Rayleigh instability for formation of droplets on a wire, the most rapidly growing mode determines the distance between jets. The dimensionless wavelength Λ of the dominant mode is expressed succinctly as a function of the "electrospinning number" Γ:

$$\Lambda = \frac{3\pi}{\Gamma + \sqrt{\Gamma^2 - 3/4}}, \tag{4}$$

Where $\Lambda = \lambda_j / l_{cap}$ and $\Gamma = l_{cap}\varepsilon E_0^2 / 2\gamma$. Here, λ_j is the wavelength of the dominant mode and thus the distance between jets emitted from the free liquid surface in this case.

3. Experimental Method

3.1 Experimental Setup

The experimental configuration was constructed as shown in Fig. 3. The wire electrode spindle consisted of two Teflon disks 3.2 cm in diameter and 0.4 cm thick held in position 6.4 cm apart (center-to-center) with a threaded rod and nuts. Two 200 μm diameter (r = 100 μm)

stainless steel wires were wrapped around the disks approximately 180^{o} apart from each other, as shown in Fig. 4.

(a)

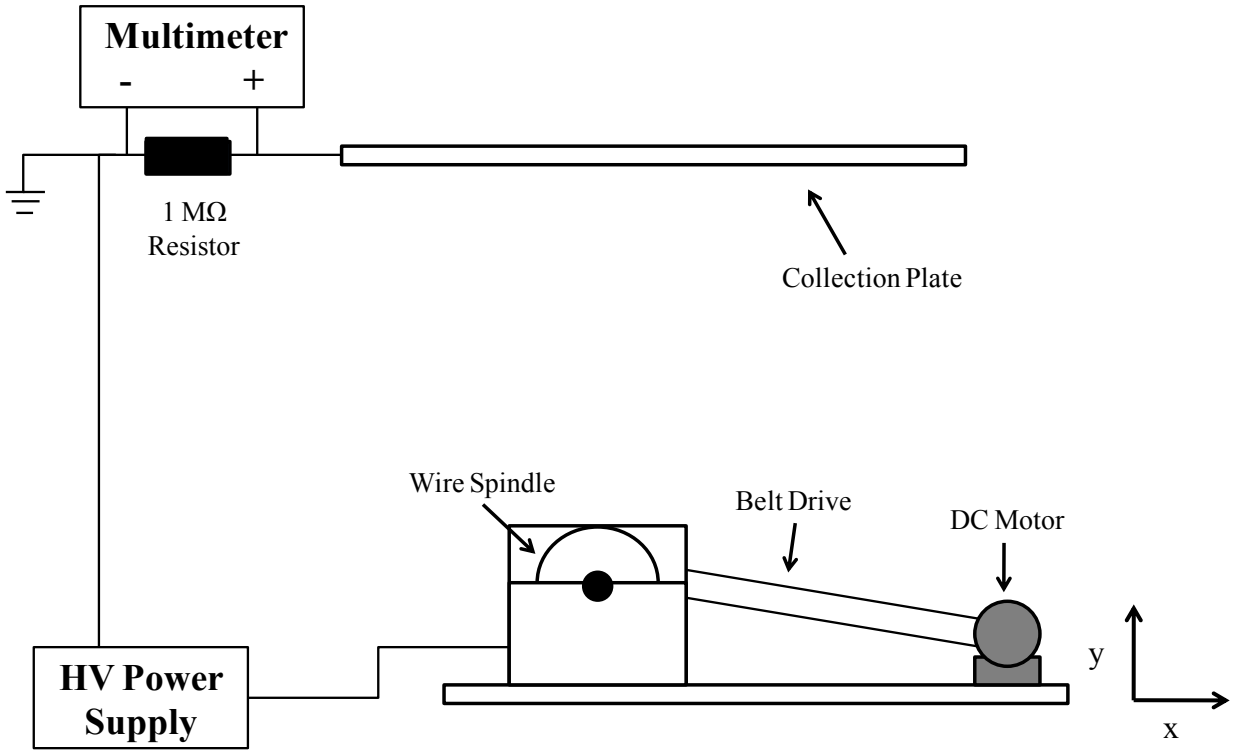

(b)

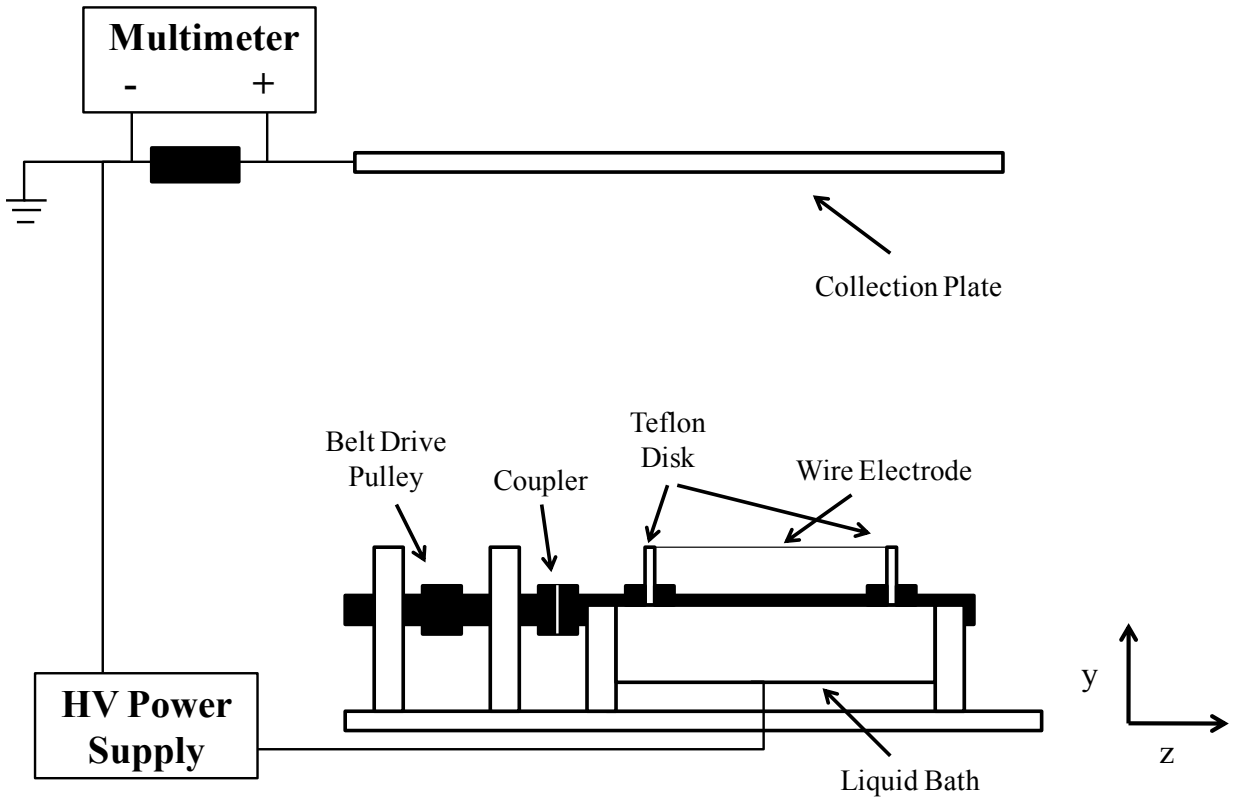

Figure 3. Apparatus for free surface electrospinning from wire electrodes. The liquid bath is connected to a high voltage power supply and the collection plate is connected to ground with a 1 MΩ resistor in series. The voltage drop across the resistor is measured and converted to an electrical current. (a) side view, parallel to spindle axis; (b) front view, perpendicular to spindle axis.

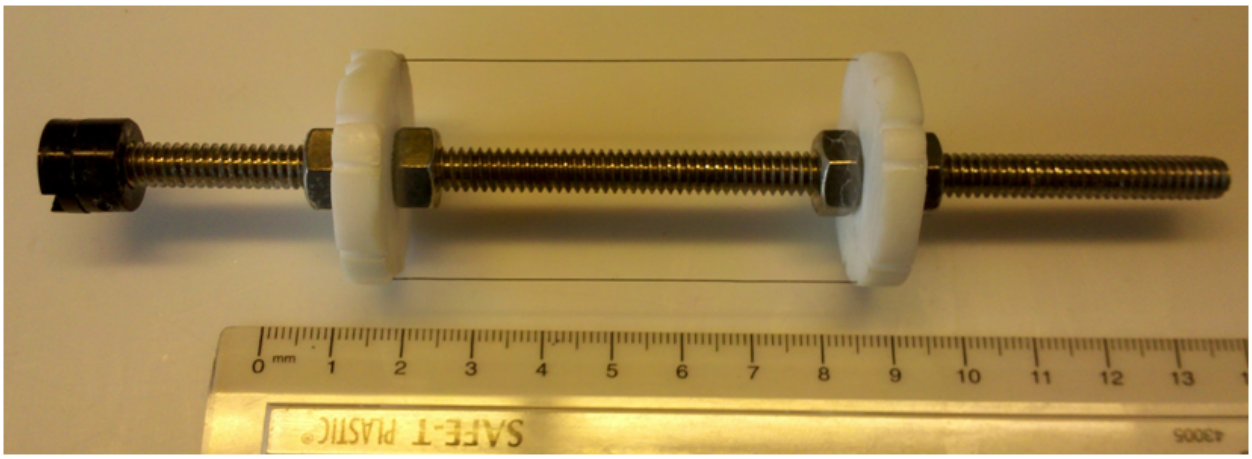

Figure 4. Image of spindle electrode with two wires 180° apart

The wire spindle was connected to a belt drive that was powered by a small DC motor (Zheng gear box motor ZGA25RP216) to allow for variable speed control. A DC power supply controlled the rotation rate of the wire spindle between 2.5 and 18 rpm. This corresponds to a wire velocity, u, of 0.4 - 3 cm/s. Using the relation, $\dot{\gamma} \approx u/z$, where z is the thickness of the liquid entrained on the wire (30-50 microns, *c.f.* section 4.1), these velocities translate to shear rates of ~100-700 s^{-1} for the wire passing through the solution bath. The wire spindle was placed in a solution bath as shown in Fig. 3, with the center of rotation positioned approximately at the surface of the bath. The solution bath was 10 cm long and 5 cm wide. A grounded collection plate was positioned above the spindle at a distance of 21.6 cm from the axis of the spindle. The grounded electrode acted as the counter electrode for the charged jets.

3.2 Solution Preparation

Two samples of polyvinylpyrrolidone (PVP) with Mw=55kDa and 1.3 MDa were obtained from Sigma Aldrich. Ethanol (solvent) was obtained from Koptec. Solutions of 2-8 wt% of 1.3MDa PVP and 10-30 wt% of 55kDa PVP in ethanol were prepared. A volume of 35

ml of each of solution was poured into the bath section of the apparatus. The solution conductivity was measured using a VWR Digital Conductivity Meter. The surface tension was measured using a Krüss K100MK2 Processor-Tensiometer. The viscosity was determined using an AGR2 Rheometer (TA instruments). Mineral oils with viscosities of 16 mPa·s and 71 mPa·s (Paragon Scientific Ltd., ISO 17025 Certified Reference Standard) were also used, as Newtonian liquid standards. The zero shear viscosity is reported in Table 1, along with other relevant properties of the fluids, since all solutions showed Newtonian behavior for shear rates less than 1000 s^{-1}.

Material	Concentration (wt% in EtOH)	Density, ρ (g/mL)	Conductivity (μS/cm)	Viscosity, η (mPa·s)	Surface Tension, γ (mN/m)	Bo	Oh
Mineral oil	–	0.89	<0.01	16	35	0.0025	0.29
	–	0.86	<0.01	71	36	0.0023	1.3
1.3 MDa PVP	2	0.79	0.05	7.3	23	0.0034	0.17
	4	0.80	0.14	21	23	0.0034	0.49
	6	0.81	0.22	53	23	0.0034	1.2
	8	0.82	0.28	72	23	0.0035	1.6
55 kDa PVP	10	0.82	7.60	7.7	23	0.0035	0.17
	20	0.85	8.78	27	23	0.0037	0.61
	30*	0.89	8.89	105	23	0.0038	2.3

Table 1: Solution properties of mineral oils and PVP/ethanol solutions, where the characteristic length, *r*, was 0.1 mm. (*): The 30 wt% solution of 55 kDa PVP in ethanol was used for electrospinning studies.

3.3 Drop size measurement.

Images of the droplets formed after de-wetting of the entrained liquid on the wire were recorded photographically (1st Vision MC-433 Fireware Camera and Quantaray AF 70-300mm f/4.0-5.6 LD Tele-Macro Lens). The equatorial height and length of the droplets, as well as the distances between droplets, were measured from photographs using ImageJ software (National

Institute of Health). The center-to-center distance λ between droplets provides a measure of the dominant mode of the Plateau-Rayleigh instability for breakup of the liquid film on the wire into droplets. A MATLAB routine was developed to calculate the shape and volume of a droplet using eq. 1 and eq. 2, to a tolerance of 0.01%. Averages were taken over at least 100 droplets for purposes of determining the droplet volume and center-to-center distance between droplets. The thickness, *z*, of the equivalent uniform annular liquid film on the wire was calculated as follows:

$$z = \left(\frac{V_d}{\pi \lambda} + r^2 \right)^{0.5} - r \tag{5}$$

3.4 Electrospinning

To induce electrospinning, the liquid solution in the bath was connected to a high voltage power supply. The wire spindle was not in direct contact to the high voltage power supply; however for sufficiently high solution conductivities (> 1 μS/cm), the surface of the bath and the wire were both observed to be at the same potential as the external power supply. The applied potential was increased until jetting was observed from the individual droplets. As the charged jets travel towards the ground electrode, the solvent evaporates, resulting in solid fibers. When the charged fibers contact the ground electrode, they displace the free charge on the grounded surface, resulting in an electric current flow. The current was assumed to be ohmic and was determined by measuring the voltage drop across a 1 MΩ resistor with a Keithley 2000 multimeter. The threshold for corona discharge from a wire electrode is predicted approximately by Peek's law for concentric cylinders [44]:

$$E_C = A\left(1 + \frac{B}{\sqrt{r}}\right) \tag{6}$$

where E_C is the electric field for onset of corona discharge, A and B are constants that depend on the temperature, pressure and nature of the surrounding medium, and r is the radius of curvature of the electrode. For atmospheric air at standard temperature and pressure, A and B are 31 kV/cm and 0.308 $cm^{1/2}$, respectively, resulting in a threshold for corona discharge of 126 kV/cm (12.6 MV/m) at the wire. Applied potentials less than 35 kV were used throughout this study to avoid corona discharge.

Because the solution bath was open to the atmosphere during electrospinning, some solvent evaporation ("solution aging") occurs over time. Electrospinning experiments were limited to 10 minutes duration to minimize the impact of solution aging on the results. The applied potential and rotation rate were the primary operating parameters varied during the electrospinning experiments. A single solution of 30 wt% 55kDa PVP in ethanol was used in all studies here. The mass of the nonwoven mat on the collector was measured after each experiment to determine the productivity of the system.

3.5 Electric Field around the Wire Electrode

A MATLAB routine was developed to calculate the static electric field around a cylinder (the wire) between two charged, finite-sized planes (the solution bath and the ground electrode), in the absence of liquid jets. First, the electric field for the finite parallel plate configuration without cylinder was solved using the following equations and boundary conditions:

$$E(x,y) = \nabla V(x,y) \tag{7a}$$

$$\begin{aligned} V(x \in (-w,+w), -d_B) &= V_{Appl} \\ V(x \in (-w,+w), d_B) &= -V_{Appl} \end{aligned} \tag{7b}$$

where w is the width of the charged liquid bath and d_B is the distance from the charged liquid bath (at potential $+V_{appl}$) to the grounded collector plate. An image plate (at potential $-V_{appl}$) was

set up symmetrically around the y=0 plane to create the isopotential at the grounded collection plate. The resulting electric field $E(x,y)$ was then used as the initial guess in order to solve for the potential and electric field due to the wire, using the following equations:

$$V_W(x,y) = k_C \lambda_C \ln\left[\frac{l_w + \sqrt{l_w^2 + d^2}}{-l_w + \sqrt{l_w^2 + d^2}}\right]$$
$$E_W(x,y) = \frac{2k_C \lambda_C}{d} \ln\left[\frac{l_w}{\sqrt{l_w^2 + d^2}}\right]$$
$$d = \sqrt{(x - x_o)^2 + (y - y_o)^2} \qquad (8a)$$

with boundary conditions

$$V(x,-y) = V_{Appl}$$
$$V(x,y) = -V_{Appl} \qquad \text{for } r = d \qquad (8b)$$

where V_{Appl} is the potential applied to the liquid bath, λ_C is the linear charge density on the wire, k_C is Coulomb's constant (8.99 x 10^9 N m^2/C^2), r is the radius of the wire, l_w is half the length of the wire electrode, and x_o and y_o are the coordinates of the center of the wire electrode. An iterative method was used to solve for the linear charge density that satisfies the boundary conditions (eq. 8b). The electric field was calculated for different positions of the wire electrode along the path of rotation.

The electric field around the wire was modeled with a wire diameter of 200 μm, with the center of rotation of the spindle positioned at x = 0 and y = -20 cm and the solution bath surface positioned at -2.5 cm < x < 2.5 cm and y = -22 cm.

Fig. 5 shows the calculated potential at an applied voltage of 30 kV with the wire electrode located at the apex of the rotation (90^o). At 0^o, the wire position is aligned with the

horizontal axis of the rotation. The electric field at the wire was calculated at different angular positions along the rotation of the spindle. The electric field at the wire was fit with a 2nd degree polynomial, shown in Fig. 6 and expressed by eq. 9, where A_1, A_2, and A_3 are -0.000204 deg^{-2} cm^{-1}, 0.0367 deg^{-2} cm^{-1} and 0.618 cm^{-1}, respectively. The right hand side of this equation is specific to the geometry of the experiment described here, but in general a functional dependence of electric field at the wire on angular position is expected to hold for other, similar geometries as well.

$$\frac{E_w(\varphi)}{V_{Appl}} = \left[A_1\varphi^2 + A_2\varphi + A_3\right] \tag{9}$$

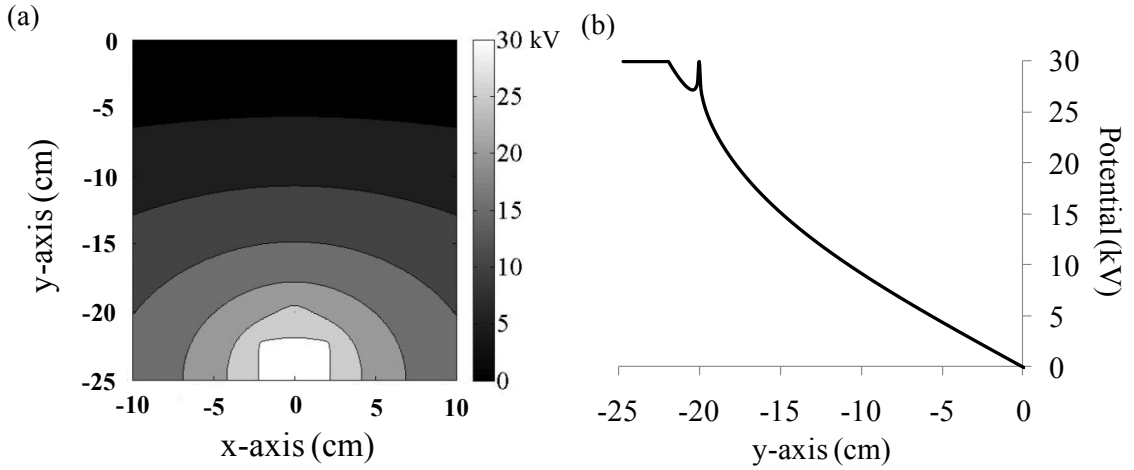

Figure 5. (a) Contour map of the computed electric potential in the xy-plane, for V_{appl} = 30 kV. (b) The potential along the y-axis at x = 0, where the bath liquid was modeled at y = -22 cm and the center wire electrode at y = -20 cm.

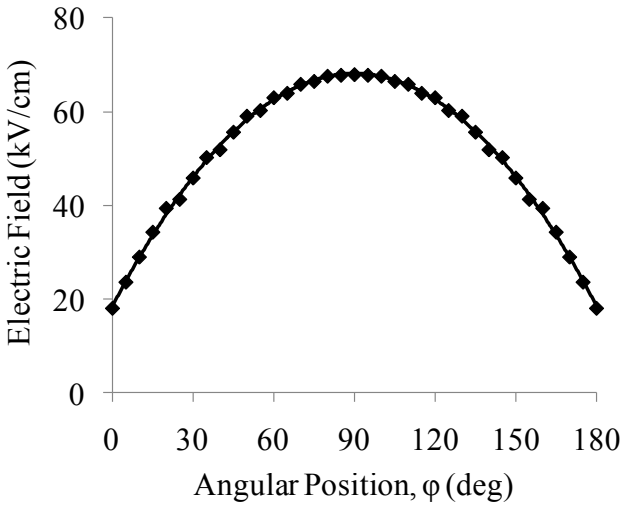

Figure 6. Local electric field at the surface of the wire at a function of angular position along the rotation at applied potential of 30 kV.

This simulation does not take into account the liquid entrainment and drop shape. The results of the MATLAB routine were confirmed with a model of the potential and electric field created using Maxwell 2D (Ansoft Corporation).

4. Results & Discussion

4.1 Liquid Entrainment

We first studied entrainment of a Newtonian liquid on a wire, oriented with its axis parallel to the liquid surface as the wire passes through the liquid surface, using two mineral oils. To our surprise, we did not find any previous reports that measured liquid entrainment in this configuration. The number and volume of oil droplets on the wire were measured for different rotation rates of the spindle, and the thickness of the entrained liquid film on the wire was calculated using eq 5. Fig. 7a shows the thickness of the annular liquid film entrained on the wire, normalized by the radius of the wire, versus the capillary number, for the two mineral oils.

The Bond numbers (Bo) for the two mineral oils were nearly the same (0.023 vs 0.025). For rotation rates from 2.5 to 15 rpm (linear velocity of 0.43-2.5 cm/sec), the Reynolds number ranges from 0.01-0.3, in accord with creeping flow conditions. Empirically, the normalized thickness was found to scale with capillary number,

$$\frac{z}{r} = aCa^{b} \tag{10}$$

where a=0.63 ± 0.067 and b=0.13 ± 0.023. The behavior follows a trend qualitatively similar to that observed by Manga and Stone [25] for an entrainment on a sphere, with the volume of liquid entrained increasing with increasing capillary number.

Next, entrainment of polymer solutions on the wire was examined for solutions of PVP (Mw=55 kDa or 1.3 MDa) in ethanol. The viscosity of the polymer solutions ranged from 10 - 160 mPa·s for each molecular weight of PVP. To obtain similar ranges of viscosity for solutions using the two different PVP's, different concentrations of polymer were studied in each case: 10-30 wt% of 55 kDa PVP and 2-8wt% of 1.3MDa PVP in ethanol. The same approach was used to determine the liquid entrainment as for the mineral oils. The results are shown in Fig. 7b. The data are well described by a similar function as the mineral oil, with the coefficients a=0.78 ± 0.03 and b=0.21 ± 0.011 determined empirically. At the low Reynolds numbers employed here, the polymer solutions behave as Newtonian fluids, with scaling behavior very similar to that for the mineral oils.

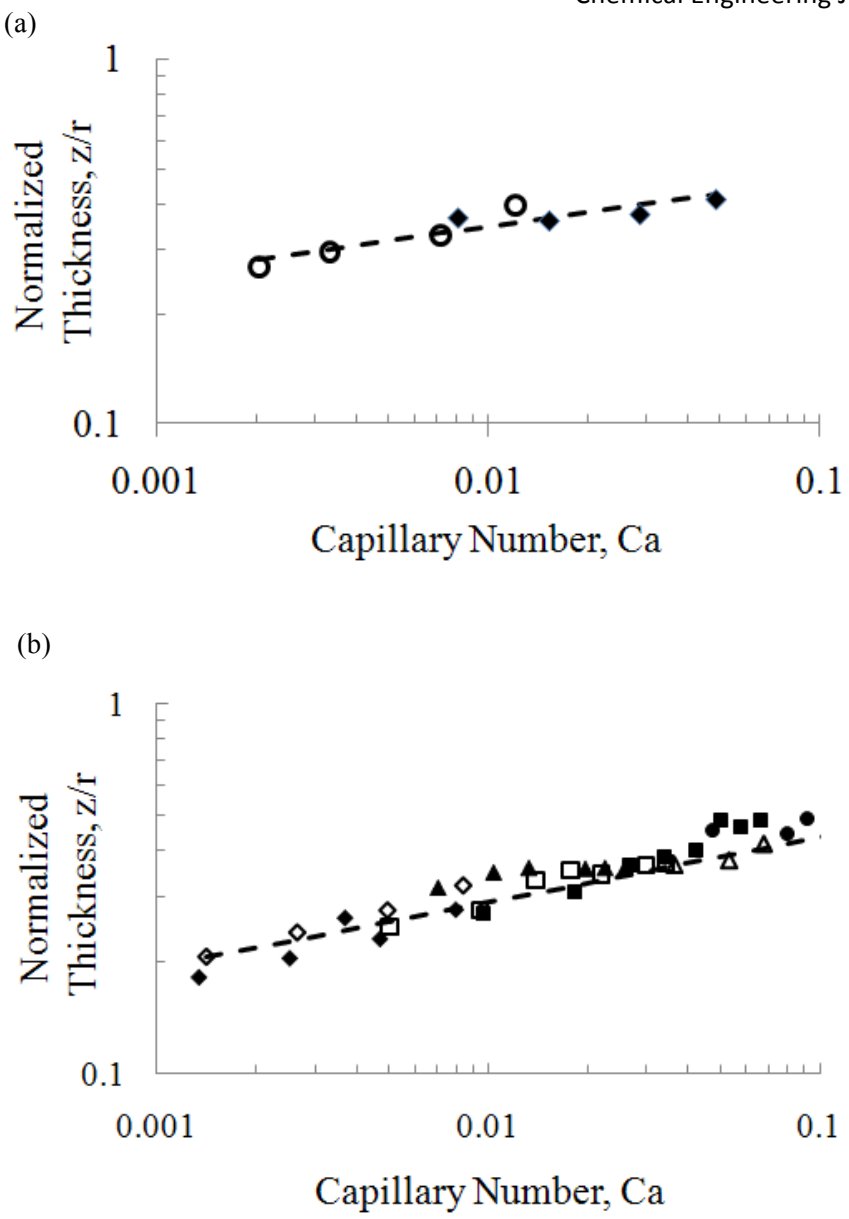

Figure 7. (a) Liquid entrainment of a Newtonian liquid under creeping flow conditions around a cylinder. Open circles: mineral oil with η=16 mPa·s and Bo=0.0023; filled diamonds: mineral oil with η=71 mPa·s and Bo=0.0025. Dashed line: linear least squares fit to the data; see text for details. Error bars are smaller than symbol size. (b) Liquid entrainment of a polymeric solution of PVP in ethanol. Open symbols: 55 kDa PVP at concentrations (in ethanol) of 10wt% (diamonds), 20 wt% (squares), and 30wt% (triangles). Filled symbols: 1.3 MDa PVP at concentrations (in ethanol) of 2 wt% (diamonds), 4 wt% (triangles), 6 wt% (squares) and 8 wt%

(circles). Bond numbers for these solutions ranged from 0.0034-0.0038. Dashed line: linear least squares fit to the data; see text for details. Error bars are smaller than symbol size.

The liquid entrainment for the polymer solutions is slightly lower at low capillary numbers (low viscosity and low rotation rates), which may be due to viscoelastic forces during the draining and rupturing of the film after the wire has moved though the interface. The polymeric solutions are shear-thinning solutions; as the draining increases in length, the shear rate increases and the liquid may eventually become less viscous. This may account for the lower entrainment of the polymer solution compared to the mineral oil.

4.2 Droplet break-up in the absence of an electric field

From the measured center-to-center distance between droplets, λ, and the calculated radius of the surface of the liquid film on the wire ($a_o=z+r$) obtained using Eq 5 for z, values of the wavelength parameter ($2\pi a_o/\lambda$) were found to be 0.50 ± 0.004 for both the mineral oils and the 1.3 MDa PVP solutions, and 0.48 ±0.02 for the 55kDa PVP solutions. Here, the subscript on a_0 indicates the radius obtained in the absence of an applied electric field. As the liquid entrainment increases, the center-to-center distance between droplets increases proportionally, in accord with theory. However, these values are significantly smaller than the limiting value of 0.69, predicted by Rayleigh [28], Tomotika [29] and Goren [27] for Newtonian liquids. In accord with Goren's analysis, the droplet break up appears to be weakly dependent on Ohnesorge number (Table 1).

4.3 Droplet break-up in the presence of an applied electric field

Different electrical potentials (0-40 kV) were applied to the liquid bath, and the grounded plate was placed 20 cm away from the apex of the rotating wire electrode. In this case, the presence of electrical charges on the surface of the liquid and the resulting electric field results in smaller distances λ between droplets on the wire with increasing applied voltage. Fig. 8 illustrates the variation of the wavelength parameter $2\pi a_0/\lambda$ with applied voltage for three different solutions, where the wavelength parameter was calculated using the value of a_o obtained at zero applied voltage for each solution. (In the presence of an applied field, the droplets were no longer symmetrical, and eq 2 could no longer be used to determine droplet volume.) This wavelength parameter was observed to increase linearly with the applied potential, $2\pi a_o/\lambda = 0.0028 V_{Appl} + 0.50$, where V_{Appl} is in units of kV, presumably due to the influence of charges on the liquid surface, for all three solutions. The center-to-center distance between droplets thus decreases with increasing applied potential and can be written as follows:

$$\lambda = \frac{2\pi a_o}{0.0028 V_{Appl} + 0.50} \tag{11}$$

Similar behavior has been observed in studies of electrowetting in microfluidic devices [45].

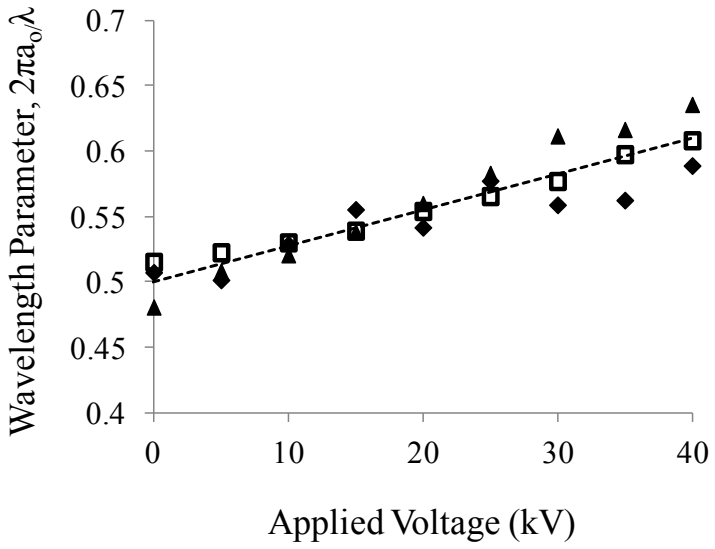

Figure 8. The variation of wavelength λ, expressed as the wavelength parameter $2\pi a_0/\lambda$, for three different polymer solutions as a function of applied voltage at a constant spindle rotation rate of 8.8 rpm. Filled diamonds: 2 wt% 1.3 MDa (a_o = 0.125 mm, Ca = 0.0047, Bo = 0.0034); Filled triangles: 4wt% 1.3 MDa (a_o = 0.131 mm, Ca = 0.013, Bo = 0.0034); open squares: 30 wt% 55 kDa PVP (a_o = 0.144 mm, Ca = 0.068, Bo = 0.0038). Dashed line: linear least squares fit to the data; see text for details.

4.4 Electrospinning and Jet Initiation

In the presence of an electric field between the charged liquid and the grounded collection plate, the droplets change from the symmetrical "barrel"-shape to a conical shape that sits asymmetrically on the charged wire in the direction of the applied field, as shown in Fig. 9. As the wire spindle rotates, the distance between the wire electrode, decorated with liquid droplets, and the ground electrode decreases, resulting in an increase in the local electric field at the wire. The increase in electrical stresses leads to formation of a cone-jet of charged solution that travels downfield (upward in Fig. 9) to the grounded plate. Jetting was observed to initiate at

an angular position that depended on the magnitude of the applied potential but not on spindle rotation rate.

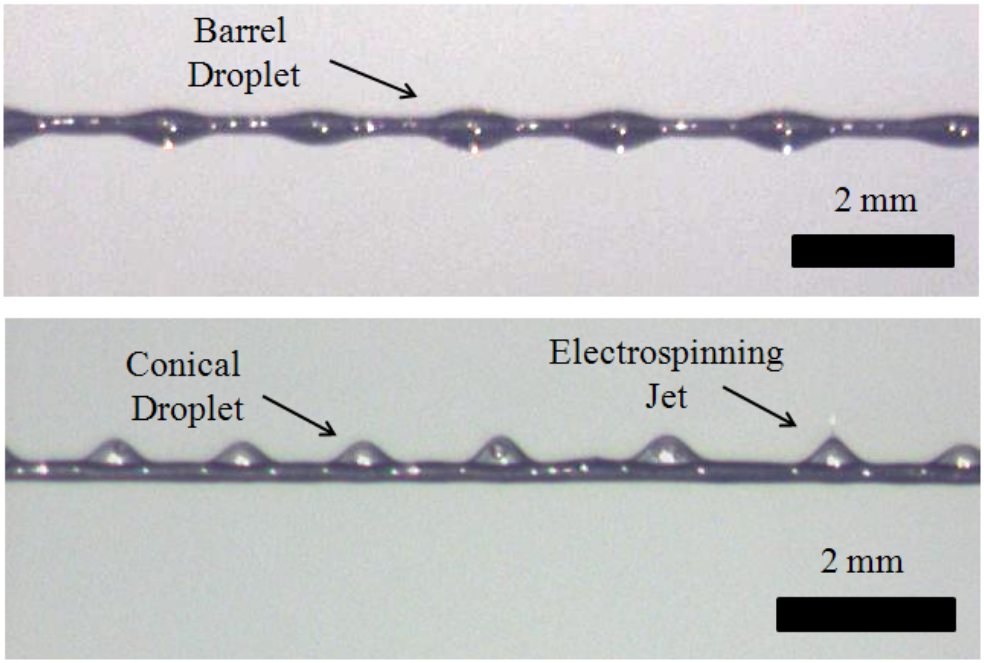

Figure 9. Optical image of droplets of polymer solution of 30 wt% 55 kDa PVP/ethanol on a wire, at a spindle rotation rate of 8.8 rpm. (a) $V_{appl} = 0$; (b) $V_{appl} = 25kV$. This photograph shows only one electrospinning jet (as indicated) while other droplets produced a conical shape, attributed to the combined effects of surface charge repulsion (similar to the Taylor cone) and attraction of the charged fluid to the grounded collection plate (as evidenced by the cones oriented preferentially downfield). Note that not all of the drops initiate jetting simultaneously.

Fig.10 shows the calculated electric field at the wire electrode (eq 9) for several values of applied voltage, upon which are overlaid the angles at which jet initiation was observed for each applied voltage. It is readily apparent that the points of initiation fall approximately on a horizontal line corresponding to 34 ± 1.3 kV/cm. Once the electric field reaches this critical value, the induced charge repulsion on the surface of the droplet overcomes the surface tension,

and jetting begins. Of course, this analysis decouples the geometry of the electric field and the local perturbations caused by the liquid droplets themselves. As a point of comparison, the analysis of Lukas *et al.* (eq 3) predicts the critical electric field for jet initiation to be 18 kV/cm for the 30wt% PVP/ethanol solution [9]. However, the model of Lukas et al assumes a perfectly conducting liquid, whereas real polymeric liquids like the solution of 30wt% PVP in ethanol have finite conductivity and are better described as "leaky dielectrics". Further work is required to understand the effects of liquid properties on the critical electric field for a given solution.

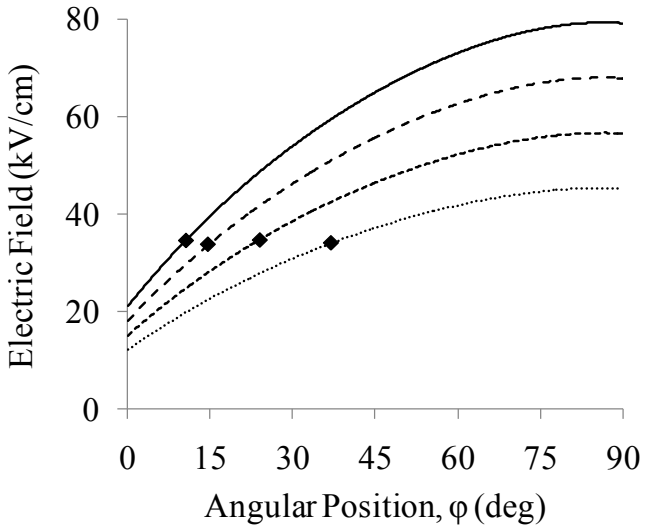

Figure 10. The calculated electric field at the wire as a function of angular position of the wire, according to the model described in Section 3.5 and summarized for the current experimental geometry by eq 9, for several values of the applied potential: 20 kV (dotted), 25 kV (short dashed), 30 kV (long dashed), and 35 kV (solid). Angular position of first jet initiation at varied applied electric potentials (solid diamond). Zero degrees corresponds to the horizon of the axis of rotation; 90^{o} corresponds to the zenith of the rotation (same geometry as electric field calculation).

4.4 Jetting Lifetime

Since the electric field is symmetric for wire positions that are displaced by equal angles of rotation with respect to the zenith of rotation (90^o), the range of rotation angles over which the conditions for jetting are satisfied may readily be estimated. For the 30wt% PVP/ethanol solution and an applied voltage of 30 kV, this condition is satisfied for angular positions from 16^o to 164^o, according to Fig. 10. To determine the actual angular range over which jetting takes place, current measurements were made; jetting was also confirmed by videography. A typical result for current measured as a function of time is shown in Fig. 11. Since conditions giving rise to corona discharge were avoided in this work, a finite current is a reliable indication of jetting.

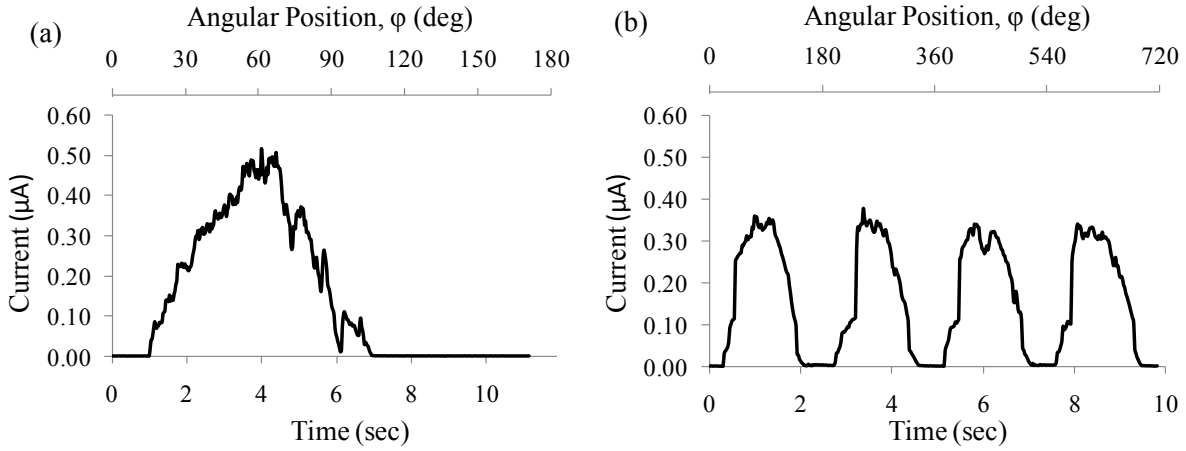

Figure 11. Current drawn from 30 wt% 55 kDa PVP/ethanol at 30 kV with rotation rates of (a) 2.5 rpm and (b) 11.8 rpm. Each rise and fall of the current signal corresponds to the super-position of jetting from several droplets on a single wire.

Using rotation rate, time can be converted to angular position of the wire relative to that of jet initiation; knowing the angular position of jet initiation, φ_I, determined by videography (Fig. 10), the current versus absolute angular position of the wire is plotted, as shown in Fig. 12.

In general, as illustrated by Fig. 12(b), the angular range of jetting was observed to increase slowly at low rotation rates, and then to saturate at high rotation rates. For example, at V_{appl}=30kV, the angular range increased with rotation rate to a value of about 148° at 7.1 rpm, corresponding to the full range of angles (from 16° to 164°) in which the electric field conditions for jetting (E_w>34 kV/cm) are satisfied. For rotation rates < 7.1 rpm, the electrical current fell back to zero before the wire had traveled to an angular position of 164^o, or 16^o above the horizon. Examination of the wire at this point confirmed that all of the liquid droplets had been converted to jets. This behavior represents the case where productivity is limited by the amount of liquid entrained on the wire: the entrained liquid was completely jetted off the wire electrode. We refer to this operating regime as "entrainment-limited". For rotation rates > 7.1 rpm, the electric current was observed to persist until the wire reached an angular position of 164°, at which point it ceased. Once the wire passed the 164^o position, the electric field was not sufficient to sustain jetting, causing the current signal to return to zero. At this point, residual liquid on the wire was confirmed visually. At high rotation rates, the current signal appeared to be symmetrical, in accordance with the previously noted symmetry of the apparatus. This behavior represents the case where electrospinning is limited by the electric field, which we refer to as the "field-limited" regime.

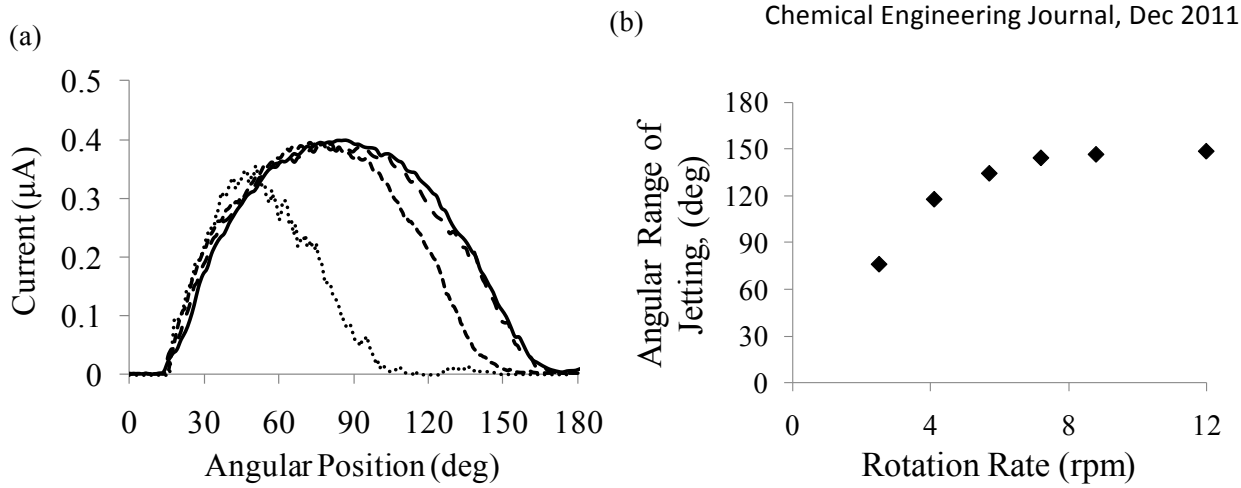

Figure 12. (a) Current drawn from 30wt% 55 kDa PVP/ethanol at 30 kV and spindle rotation rates of 2.5 rpm (dotted), 5.6 rpm (short dashed), 8.8 rpm (long dashed), and 11.8 rpm (solid) as a function of wire position. (b) Angular range of jetting versus rotation rate for an applied voltage of 30 kV (solid diamond).

4.5 Lifetime of a Single Jet and Distance between Jets

It is worth noting that, in general, the numerous droplets on the wire do not jet simultaneously, nor do they jet one at a time. To understand the distribution of jetting along the arc of rotation of the wire, jets from individual droplets were examined. For this purpose, the wire was covered with insulating tape so that ~1 cm of the bare wire remained exposed. This length allows for 4-5 droplets to form on the exposed portion of the wire. Using photography, current measurements were synchronized to measure the jetting of liquid from individual droplets; with such a short portion of exposed wire, no two droplets were observed to jet simultaneously. The current profile for jets initiated at different angular positions were observed to be relatively similar, so for subsequent analysis, it is assumed that this profile is a common feature of all the jets for a specific applied voltage. Fig. 13 shows the single jet current versus time, averaged over at least 10 jets, for an applied voltage of 30 kV and several rotation rates.

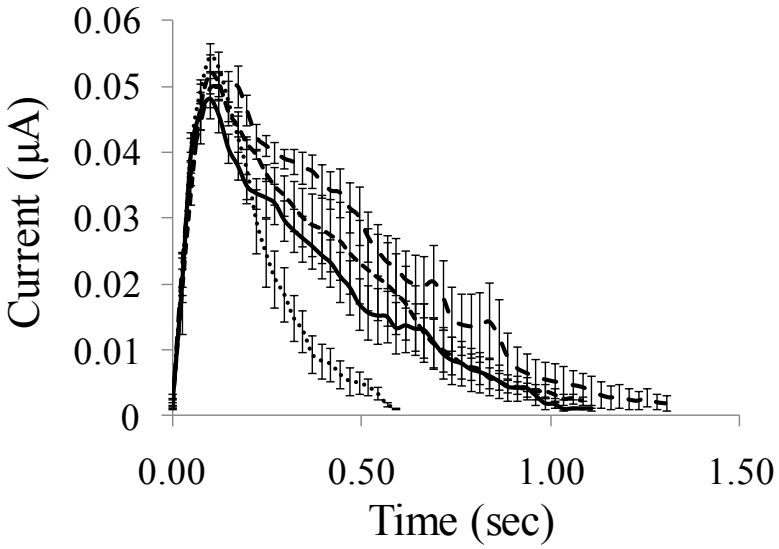

Figure 13. The average current drawn from a single droplet at 30 kV at varying rotation rates: 2.5 rpm (dotted) 5.6 rpm (short dashed), 8.8 rpm (long dashed) and 11.8 rpm (solid line). Error bars correspond to one standard deviation, determined from averaging over measurements of at least 10 single jets.

The average single jet current profile was used to extract the distribution of jets as a function of the angular position of the wire. The current profile from a wire, $i_w(t)$, (shown in Fig. 12) can be expressed as a convolution of the single jet current profile, $i_s(t)$ (shown in Fig. 13) and a jet distribution function $j(t)$ that describes the number of jets emitted from the droplets on the wire as the wire travels through its arc of rotation:

$$i_w(t) = (j * i_s)(t) = \int_0^\infty j(\tau) i_s(t-\tau) d\tau \qquad (12)$$

Given both $i_w(t)$ and $i_s(t)$ from current measurements as described above, $j(t)$ can be obtained by standard deconvolution techniques (e.g. Matlab). Fig. 14 shows the linear jet density distribution function after noise filtering and dividing by the total length of wire, for several rotation rates at an applied voltage of 30 kV. At each rotation rate, the linear jet density distribution function is

nonzero over a finite time, $0 \leq t \leq b$, as shown in Fig 14. This time window corresponds to the time when conditions are satisfied for jet initiation, namely, when both electric field is greater than the critical value (34 kV/cm in this instance, field limit) and there remains some entrained liquid on the wire (entrainment limit). The value of b can also be equated with the time of spinning for a single wire, t_w, (Fig. 11) minus the lifetime of a single jet, t_J (Fig. 13).

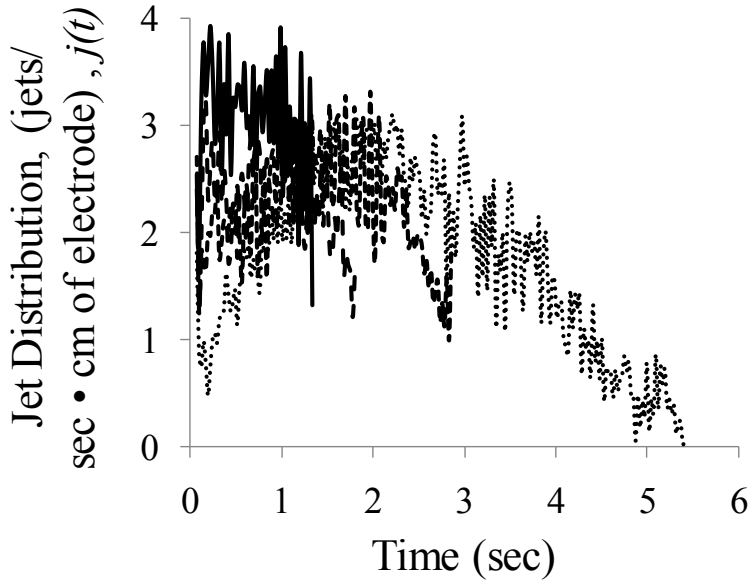

Figure 14. The linear jet density distribution function, $j(t)$, in units of $s^{-1}cm^{-1}$, at several rotation rates: 2.5 rpm (dotted) 5.6 rpm (short dashed), 8.8 rpm (long dashed) and 11.8 rpm (solid line). Deconvolution was performed using the Matlab *deconv* function, with a time step of 0.0246 sec. In the case of 2.5 rpm, deconvolution was performed by spectral division, since the deconvoluted signal became unstable using the Matlab *deconv* function. After deconvolution, the signal $j(t)$ was noise filtered using a moving average of 5 data points, and converted to a linear density distribution by dividing by the length of the wire electrode (6.4 cm).

Once the linear jet density distribution function is determined, the total number of jets, n_J, emitted from a single wire was calculated by integrated over the observed jetting time, b.

Equivalently, the linear jet density distribution function for each rotation rate can be expressed as a function of angular position, through a transformation of variables $(\varphi = \varphi_I + t\Omega)$:

$$n_J = \int_0^b j(t)dt = \frac{1}{\Omega}\int_{\varphi_I}^{\varphi_I + b\Omega} j(\varphi)d\varphi \tag{13}$$

where Ω is the rotation rate with units of degrees/sec.

j(t) expressed the linear density of jets that are *initiated* as a function of time (or angular position) during the rotation of the spindle. Each jet has a finite lifetime. The linear density of *concurrent* jets as a function of angular position, $n_C(\varphi)$, was calculated as a moving integral over the angular sweep of a single jet, Ωt_J:

$$n_C(\varphi) = \frac{1}{\Omega}\int_{\varphi - \Omega t_J}^{\varphi} j(\varphi')d\varphi' \tag{14}$$

where $[\varphi_I > \varphi > \varphi_I + \Omega t_w]$. In addition, it is possible to rearrange Eq. 13 and Eq. 14 and solve for n_J in terms of n_C.

$$n_J = \frac{1}{\Omega t_J}\int_{\varphi_I}^{\varphi_I + \Omega t_w} n_C(\varphi)d\varphi \tag{15}$$

Fig. 15a shows the linear density of concurrent jets as a function of angular position. At low rotation rates (i.e. where entrainment is limiting), the maximum number of concurrent jets occurs below the apex of the rotation and drops to zero before reaching an angular position 164° (E_w ~ 34 kV/cm), which confirms the depletion of droplets during the rotation of the electrode. However, at high rotation rates (i.e. where the electric field is limiting), the maximum number of concurrent jets occurs close to the apex and drops to zero at an angular position of 164°, which confirms that a sufficient number of droplets was created to maintain jetting over the largest permissible range of rotation. It is important to note that in Fig. 15, the field-limited regime

shows symmetry around 90°, and that this symmetry breaks down in the entrainment-limited regime. The symmetry of the linear density of concurrent jets observed in the field-limited regime is similar to the symmetry exhibited by the electric field around the apex of the rotation.

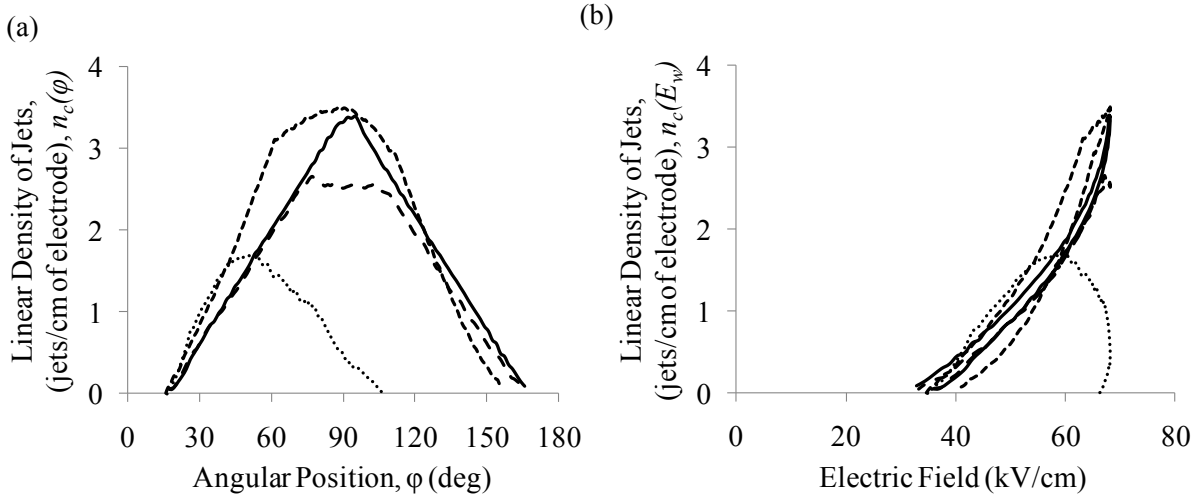

Figure 15. (a) The linear density of jets as a function of angular position and (b) electric field at different rotation rates: 2.5 rpm (dotted) 5.6 rpm (short dashed), 8.8 rpm (long dashed) and 11.8 rpm (solid line).

As discussed earlier (*c.f.* Section 2.4), the main driving force behind electrospinning is believed to be the surface charge repulsive forces, which in turn are determined primarily by the electric field. Using the results of the electric field modeling (Eq. 9), the linear density of concurrent jets ($n_C(\varphi)$) was transformed from a function of angular position to a function of electric field. The results of this transformation are shown in Fig. 15b for both the approach to and retreat from the apex. Initially, the linear density of concurrent jets exhibits a common profile during approach to the apex, regardless of rotation rate. However, for low rotation rates (2.5 rpm in Fig 15b) the linear density of concurrent jets begins to deviate from the common behavior observed at high rotation rates; this behavior is indicative of the depletion of droplets as

the wire electrode rotates in the entrainment-limited regime, which is also reflected in a lower linear density of jets. At high rotation rates (8.8 rpm and above, where jetting is field-limited), the linear density of concurrent jets exhibits a nearly universal behavior as a function of electric field at the wire. This is similar to Lukas' model [9] and suggests that the linear density of jets (i.e λ_j^{-1} in the parlance of Section 2.4) has a strong and universal dependence on the electric field.

The linear density of the jets for the solution of 30wt% 55kDa PVP in ethanol was calculated by fitting a second degree polynomial to the field-limited cases (8.8 rpm and 11.8 rpm), where E_w is in units of kV/cm of wire.

$$n_C(E_w) = 0.00192E_w^{\,2} - 0.118E_w + 1.95 \qquad \text{[jets/cm]} \qquad (16)$$

4.6 Productivity

Productivity is defined here as the total mass of fiber produced per unit time per unit length of electrode, and is readily measured as the rate of mass accumulated on the collector during an experiment. Each of the several steps that occur as part of the free surface electrospinning process described here, i.e. liquid entrainment, breakup into droplets of specified volume and spacing on the wire, and jet initiation/termination, potentially plays a role in setting the productivity of the process. The liquid entrainment step determines the maximum amount of liquid loaded onto a single wire. The Plateau-Rayleigh instability determines the spacing between droplets that form on the wire, which in turn fixes both the number and volume of droplets into which the entrained liquid film breaks up. The time during which jetting occurs is dependent on the operating parameters (applied potential and rotation rate) and system geometry.

To predict the productivity, it is clear from the preceding sections that we must consider two possible operating regimes. In the case of the entrainment-limited regime, productivity is

simply determined by the amount of liquid entrained on the electrode, obtained from eqs 5 and 10:

$$P_E = \pi\Omega C r^2 \left[\left(aCa^b + 1 \right)^2 - 1 \right], \tag{17}$$

where C is the concentration of polymer, in mass per unit volume. Since productivity is expressed per unit length of wire, this relation holds equally well for a single wire of length l_w or m wires of length l_w/m, so long as the m wires are not close enough to interfere with each other. In eq 17, it is assumed that the amount of liquid entrained on the wire does not vary with applied voltage.

In the case of the field-limited regime, productivity is determined by the number of jets that are emitted while the field strength at the wire exceeds the critical value. To determine this, the number of droplets that are converted to jets is estimated by application of Eqs. 5, 9, 10, 15 and 16, with the upper bound for jetting set at $180^o - \varphi_I$. For a particular system configuration and applied voltage, φ_I can be estimated by the construction shown in Fig 10. Fig 12 shows that jetting only occurs when the electric field at the wire is greater than the critical electric field for jet initiation.

$$P_F = V_d \Omega C n_J = \frac{\pi\lambda r^2 C}{t_J} \left[\left(aCa^b + 1 \right)^2 - 1 \right] \frac{\int_{\varphi_I}^{180°-\varphi_I} n_C \left(E_w(\varphi') \right) d\varphi'}{360°} \tag{18}$$

Here, we have again assumed that the amount of liquid entrained on the wire does not vary with applied voltage, but is only a function of capillary number. The center-to-center distance between droplets, λ, varies with applied voltage according to eq. 11. We have also estimated the average lifetime of a jet, t_J, to be 1.2 seconds, based upon the results in Fig. 13. For purposes of predicting productivity, we assume that this lifetime does not change significantly with applied voltage, since similar current profiles for single jets were observed at different angular positions

(also, local electric field) of the wire, as discussed in connection with Fig 13. As was the case for P_E, eq 19 for P_F is valid for any number of wires, so long as the wires are not close enough to interfere with one another.

Fig. 16 shows the measured productivity and the predicted productivity calculated by Eq. 17, for the entrainment-limited regime, and Eq. 18, for the field-limited regime, for a 30 wt% solution of PVP in ethanol at several different applied voltages and rotation rates. For the productivity of the entrainment-limited regime, we have assumed that the applied voltage does not affect entrainment. However, we know from Fig 8 that the spacing between droplets decreases with increasing applied voltage. At the highest applied potential (35 kV), the measured productivity is greater than that predicted by P_E in eq 17. This suggests that the total amount of liquid entrained increases with applied voltage, by an amount that cannot be independently determined using our symmetrical droplet analysis method. We speculate that this increase in entrainment occurs primarily due to a reduction in effective surface tension at high voltages due to the compensatory effect of repulsion between charges induced on the surface of the liquid. However, the electric field may also play a role, through the introduction of electrostatic forces that alter the draining of liquid from the wire as it exits the bath. Quantification of these effects is a topic for future studies.

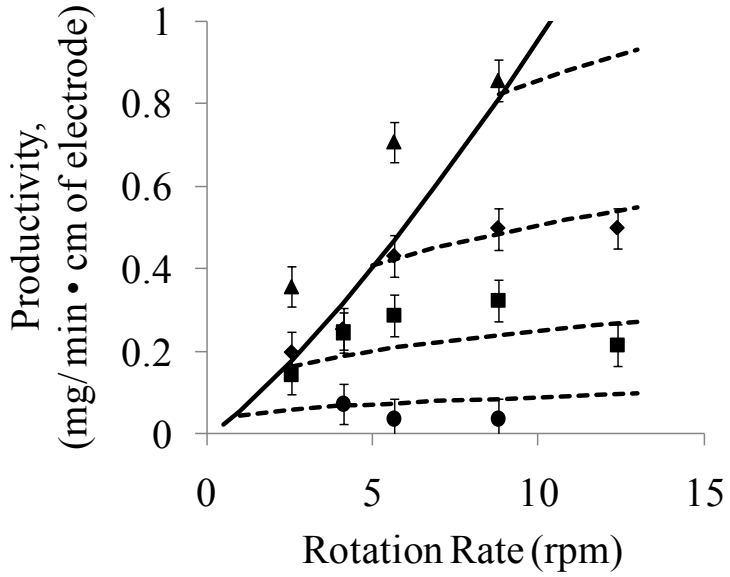

Figure 16. Experimentally observed productivity (filled symbols) and the productivity calculated from eq 17 (entrainment-limited, solid line) and eq 18 (field-limited, dashed line) as a function of rotation rate, for 30 wt% 55 kDa PVP in ethanol at different applied voltages: 20 kV (circle), 25 kV (square), 30 kV (diamond) and 35 kV (triangles). Liquid entrainment and lifetime of a single jet were assumed to be independent of applied voltage.

For the case of the field-limited regime, the predicted productivity P_F shows reasonable agreement with the measured productivity. The linear density of concurrent jets, $n_C(\varphi)$, was explicitly determined by the experiments performed at an applied voltage of 30kV. Nevertheless, the model is fairly successful in predicting productivities at other applied voltages as well. The main limitations are our assumptions that the amount of fluid entrained and the lifetime of a single jet do not vary with applied voltage. The latter is justified at least in part by the data in Fig 13, where the single jet current profiles were found to vary only slightly with angular position (or local electric field). To the extent that entrainment increases with applied voltage, the prediction for productivity in the field-limited regime given by Eq 18 provides a lower bound.

Based on the observations of the system, it is desirable to operate the system at high potentials and high rotation rates to increase the productivity of the process. The angular of rotation for which the electric field at the wire exceeds the critical electric field increases, thus providing more time for the droplets to form jets at a given rotation rate. The productivity is increased at high rotation rates due to increased liquid entrainment. However, while higher rotation rates mean more liquid entrained on the wire, it also means less time for the droplets that form from this liquid to jet, so that above a certain rotation rate, the process again becomes field-limited. We suggest that, given a desired electric field for electrospinning, the rotation rate that signals the transition from entrainment-limited operation to field-limited operation may offer the best trade-off in terms of productivity, equipment cost and operational complexity.

Only a single wire diameter was investigated here. Nevertheless, the effect of varying wire diameter can be inferred from the correlations obtained. Based on equation 10, the volume of liquid entrained on the wire should increase with increasing wire diameter. According to equation 11, the subsequent Plateau-Rayleigh instability should result in fewer, larger droplets on the wire. However, increasing the wire diameter implies a decrease in the curvature of the wire, resulting in a decrease in the local electric field at the wire surface according to equation 8 and larger angular positions for jet initiation. Based on these trends, we would predict that productivity increase in the entrainment limited regime, but the onset of the field limited regime would occur at lower rotation rates.

4.7 Fiber Diameter and Morphology

Scanning electron microscopy was used to examine the fiber diameter and uniformity and to confirm the nonwoven nature of the electrospun mats. Figure 18 shows a typical micrograph. Samples were sputtered with 30 nm of gold/palladium. The size distributions of electrospun

fibers were determined by measuring at least 100 fiber diameters with ImageJ software. Table 2 shows the means and standard derivations of the electrospun fiber diameters from a solution of 30wt% 55 kDa PVP in EtOH processed with different spindle rotation rates and applied voltages. These size distributions are typical for the PVP/EtOH electrospun materials. Changes in these process parameters had little effect on the fiber diameters or distributions. The fibers were observed to by uniform in all cases, and no deviation from the usual, randomly oriented nonwoven morphology was noted.

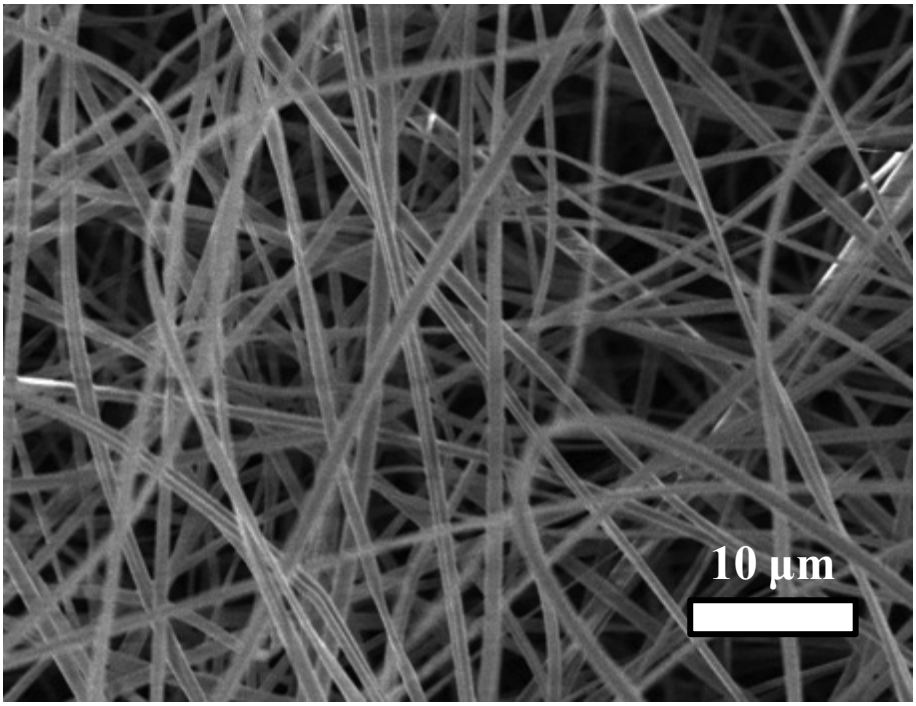

Figure 17. Scanning electron micrograph of elecrospun mat of 30wt% 55kDa PVP in EtOH at applied voltage of 25 kV, rotation rate of 8.8 rpm and working distance of 20 cm.

(a) Rotation rate = 5.7 rpm	
Applied Voltage (kV)	Fiber Diameter (nm)
20	749 ± 138
25	792 ± 195
30	778 ± 210
35	775 ± 218

(b) Applied voltage = 25 kV	
Rotation Rate (rpm)	Fiber Diameter (nm)
2.5	898 ± 258
5.7	792 ± 195
7.3	775 ± 191
8.8	711 ± 183

Table 2: (a) Means and standard derivations of electrospun fiber diameters for different applied voltages at a constant rotation rate of 5.7 rpm and (b) different rotation rates at a constant applied voltage of 25kV(right) of 30wt% 55kDa PVP in EtOH at working distance of 20 cm.

5. Conclusion

A laboratory scale version of free surface electrospinning from a rotating wire electrode spindle has been designed and analyzed for productivity. A preliminary model for entrainment of a Newtonian liquid on a thin cylinder under creeping flow conditions was presented. This model serves as a first step towards a more general model that includes the effects of viscoelasticity (for non-Newtonian liquids) and electrical forces (for leaky dielectrics).

The electric field in the absence of jetting was determined analytically for the current equipment configuration and used as an aid to interpret the experimental results. From this it was found that there exists a critical electric field strength at the wire that defines the angular range for jetting. In the case of 30wt% PVP (55 kDa) in ethanol, the critical electric field for jet initiation was determined to be approximately 34 kV/cm. This result paves the way for future work to understand how the critical electric field for jetting depends on fluid properties. Our analysis reveals two limiting regimes for productivity. In the first regime, productivity is limited by the amount of liquid entrained on the wire. The second regime occurs with high spindle rotation rate and low applied potential, in which productivity is limited by the angular range, and

hence time span, over which jetting occurs. Unlike conventional electrospinnning, the productivity of free surface electrospinning is not controlled by the flow rate from a pump. It is our hope that the analysis presented here provides a framework for understanding how productivity can be characterized and optimized as a function of equipment geometry, fluid properties and applied voltage in the case of free surface electrospinning from a wire.

Acknowledgements

This work is funded by the MIT-Novartis Center for Continuous Manufacturing.

References

[1] S.A. Theron, E. Zussman, A.L. Yarin, Experimental investigation of the governing parameters in the electrospinning of polymer solutions. Polymers 45 (2004) 2017-2030.
[2] Y.Yang, Z. Jia, Q. Li, L. Hou, J. Liu, L. Wang, Z. Guan, M. Zahn, A shield ring enhanced equilateral hexagon distributed multi-needle electrospinning spinneret, IEEE Trans. Dielectric and Insulation. 17 (2010) 1592-1601.
[3] F.-L. Zhou, R. –H. Gong, I. Porat, Three-jet electrospinning using a flat spinneret, J. Mater. Sci. 44 (2009) 5501-5508.
[4] S.A. Theron, A.L. Zussman, E. Kroll, Multiple jets in electrospinning: Experiment and modeling, Polymer 46 (2005) 2889-2899.
[5] O.O. Dosunmu, G.G. Chase, W. Kataphinan, D.H. Reneker, Electrospinning polymer nanofibers from multiple jets on a porous tubular surface, Nanotech. 17 (2006) 1123-1127.
[6]G.H. Kim, Y.S. Cho, W.D. Kim, Stability analysis for multi-jets electrospinning process modified with a cylindrical electrode, Euro. Poly. J. 42 (2006) 2031-2038.
[7] H.Y. Kim, J.C. Park, Conjugate electrospinning devices, conjugate nonwoven and filament comprising nanofibers prepared by using the same, US Patent WO2007035011 (2007).
[8] J.S. Varabhas, G.G. Chase, D.H. Reneker, Electrospun nanofibers from a porous hollow tube, Polymer 49 (2008) 4226-4229.
[9] D. Lukas, A. Sarkar, P. Pokorny, Self-organization of jets in electrospinning for free liquid surface: a generalized approach, J. Appl. Phys. 103 (2008) 084209.
[10] A.L. Yain, E. Zussman, Upward needleless electrospinning of multiple nanofibers, Polymers 45 (2004) 2977-2980.
[11] T. Miloh, B. Spivak, A.L. Yarin, Needleless electrospinning: Electrically driven instability from the free surface of a spherical liquid layer, J. Appl. Phys. 106 (2009) 114910-114910-8.
[12] E. Kostakova, l. Meszaros, J. Gregr, Composite nanofibers produced by modified needleless electrospinning, Mater. Lett. 63 (2009) 2419-2422.
[13] O. Jirsak, P. Sysel, F. Sanetrnik, J. Hruza, J. Chaloupek, Polyamic acid nanofibers produced by needleless electrospinning, J. Nanomaterials, 2010 (2010) ID842831.
[14] H. Niu, T. Lin, X. Xang, Needleless electrospinning: A comparison of cylinder and disk nozzles, J. Appl. Poly. Sci. 114 (2009) 3524-3530.
[15] X. Wang, H. Niu, T. Lin, Needleless electrospinning of nanofibers with a conical wire coil, Polymer Engin. Sci. 49 (2009) 1582-1586.
[16] B. Lu, Y. Wang, Y. Liu, H. Duan, J. Zhou, Z. Zhang, Y. Wang, X. Li, W. Wang, W. Lan, E. Xie, Superhigh-throughput needleless electrospinning using rotary cone as spinneret, Small 6 (2010) 1612-1616.
[17] T. B. Green, Apparatus and method for reducing solvent loss for electro-spinning of fine fibers, US Patent US7815427.
[18] Y. Liu, J-. H. He, Bubble elecrtospinning for mass production of nanofibers, Int. J. Nonlinear Sci. Num. Simulation 8 (2007) 393-396.
[19] J.S. Varabhas, S. Tripatanasuwan, G.G. Chase, D.H. Reneker, Electrospun jets launched from polymeric bubbles, J. Engin. Fibers Fabrics 4 (2009) 46-50.
[20] S. Hartland, The profile of a draining film between a rigid sphere and a deformable fluid-fluid interface, Chem. Engng Sci. 24 (1969)
[21] I. Cohen, H. Li, J. L. Hougland, M. Mrksich, S.R. Nagel, Using selective withdrawal to coat microparticle, Science 292 (2001) 265-267.

[22] I. Cohen, S.R. Nagel, Scaling at the selective withdrawal transition through a tube suspend above the fluid surface, Phys. Rev. Lett., 88 (2002) 074501-1.
[23] M.H. May, M.V. Sefton, Conformal coating of small particles and cell aggregates at a fluid-fluid interface, Annals of the New York Academy of Sciences, 875 (1999) 126-134.
[24] A.S. Geller, S.H. Lee, L.G. Leal, The creeping motion of a spherical particle normal to a deformable interface, J. Fluid Mech., 169 (1986) 27-69.
[25] M. Manga, H.A. Stone, Low reynolds number motion of bubbles, drops and rigid spheres through fluid-fluid interfaces, J. Fluid Mech., 287 (1995) 279-298.
[26] S.H. Lee, L.G. Leal, The motion of a sphere in the presence of a deformable interface: II. A numerical study of the translation of a sphere normal to an interface, J. Colloid Interface Sci., 87 (1982) 81-106.
[27] S.L. Goren, The instability of an annular thread of fluid, J. Fluid Mech., 12 (1962) 309-319.
[28] L. Rayleigh, On the instability of a cylinder of a viscous liquid under capillary force, Phil. Mag. 34 (1879) 145.
[29] S. Tomotika, On the instability of a cylindrical thread of a viscous liquid surrounded by another viscous liquid, Proc. Roy. Soc. A. 150 (1935) 322.
[30] A.L. Yarin, A. Oron, P. Rosenau, Capillary instability of thin liquid film on a cylinder, Phys. Fluids A 5 (1993) 91-98.
[31] B.J. Carroll, The accurate measurement of contact angle, phase contact area, drop volume, and laplace excess pressure in drop-on-fiber systems, J. Colloid Interface Sci., 57 (1976) 488-495.
[32] B.J. Carroll, Equilibrium conformations of fluid drops on thin cylinders under forces of capillary. A theory for the roll-up process, Langmuir 2 (1986) 248-250.
[33] B. Song, A. Bismarck, R. Tahhan, J. Springer, A generalized drop length-height method for setermination of contact angle in drop-on-fiber systems, J. Colloid Interface Sci., 197 (1998) 68-77.
[34] M.S. Hohman, M. Shin, G.C. Rutledge, M.P. Brenner, Electrospinning and electrically forced jets I: Stability theory, Phys. Fluids 13 (2001) 2201-2220.
[35] M. S. Hohman, M. Shin, G.C. Rutledge, M.P. Brenner, Electrospinning and electrically forced jets II: Applications, Phys. Fluids 13 (2001) 2221-2236.
[36] Y.M. Shin, M.M. Hohman, M.P. Brenner, G.C. Rutledge, Electrospinning: A whipping fluid jet generates submicron polymer fibers, Appl. Phys. Lett. 78 (2001) 1149-1151.
[37] J.H. Yu, S.V. Fridrikh, G.C. Rutledge, The role of elasticity in the formation of electrospun fibers, Polymer 47 (2006) 4789-4797.
[38] J.J. Feng, The stretching of an electrified non-Newtonian jet: A model for electrospinning, Phys. Fluids 14 (2002) 3912-3926.
[39] C.P. Carroll, Y.L. Joo, Axisymmetric instabilities of electrically driven viscoelastic jets, J. Non-Newt. Fluid Mech. 153 (2008) 130-148.
[40] S.V. Fridrikh, J.H. Yu, M.P. Brenner, G.C. Rutledge, Controlling the fiber diameter during electrospinning, Phys. Rev. Lett. 90 (2003) 145502.
[41] M.E. Helgeson, K.N. Grammatikos, J.M. Deitzel, N.J. Wagner, Theory and kinematic Mmeasurements of the mechanics of stable electrospun polymer jets, Polymer 49 (2008) 2924-2936.
[42] A.M. Gañán-Calvo, Cone-jet analytics extension of Taylor's electrostatic solution and the asymptotic universal scaling laws in electrospraying, Phys. Rev. Letts. 79 (1997) 217-220.

[43] P.K. Bhattacharjee, T.M. Schneider, M.P. Brenner, G.H. McKinley, G.C. Rutledge, On the measured current in electrospinning, J. Appl. Phys. 107 (2010) 044306.
[44] FW. Peek, Dielectric Phenomena in High Voltage Engineering., McGraw-Hill, New York, 1929.
[45]H. Gu, F. Malloggu, S.A. Vanapalli, F. Mugele, Elecrtowetting-enchanced microfluidic device for drop generation, Appl. Phys. Lett. 93 (2008) 183507.